Supplementary Information for:

Near- and Far-Field Observation of Phonon Polaritons in Wafer Scale Multilayer Hexagonal Boron Nitride Prepared by Chemical Vapor Deposition

Eugenio Calandrini, Kirill Voronin, Osman Balci, Sachin M. Shinde, Subash Sharma, Maria Barra Burillo, Andrei Bylinkin, Felix Casanova, Luis E. Hueso, Andrei Chuvilin, Clifford McAleese, Ben R. Conran, Xiaochen Wang, Kenneth Teo, Valentyn S. Volkov, Andrea C. Ferrari, Alexey Y. Nikitin, and Rainer Hillenbrand*

Supplementary Section 1. Transmission Electron Microscopy (TEM) and Electron Energy Loss Spectroscopy (EELS) of CVD h-BN multilayers.

Figure S1a and b show high-resolution TEM images of a stacked ML-hBN of about 2 nm thickness. The hBN layers are visible in profile due to folding, which results in rounded edges (marked in Figure S1), with the atomic layers parallel to the electron beam (as sketched in Figure S1c). We find that the multilayer structure is well formed but that the number of atomic layers within the same multilayer can change. We count 3 to 4 and 9 to 10 atomic layers in Figure S1a and b, respectively, which show images of the same sample. The surface of the sample shows some amorphous material. Additionally, we find interlayer defects (see area marked by the orange rectangle in Figure S1c) which may originate from the irregular stacking along the grain boundaries. This information, together with the Moirè pattern observed in Figure 1b of the main text, lets us assume that polycrystalline domains exist independently in every layer and the grain boundaries do not propagate through the whole thickness of the multilayer.
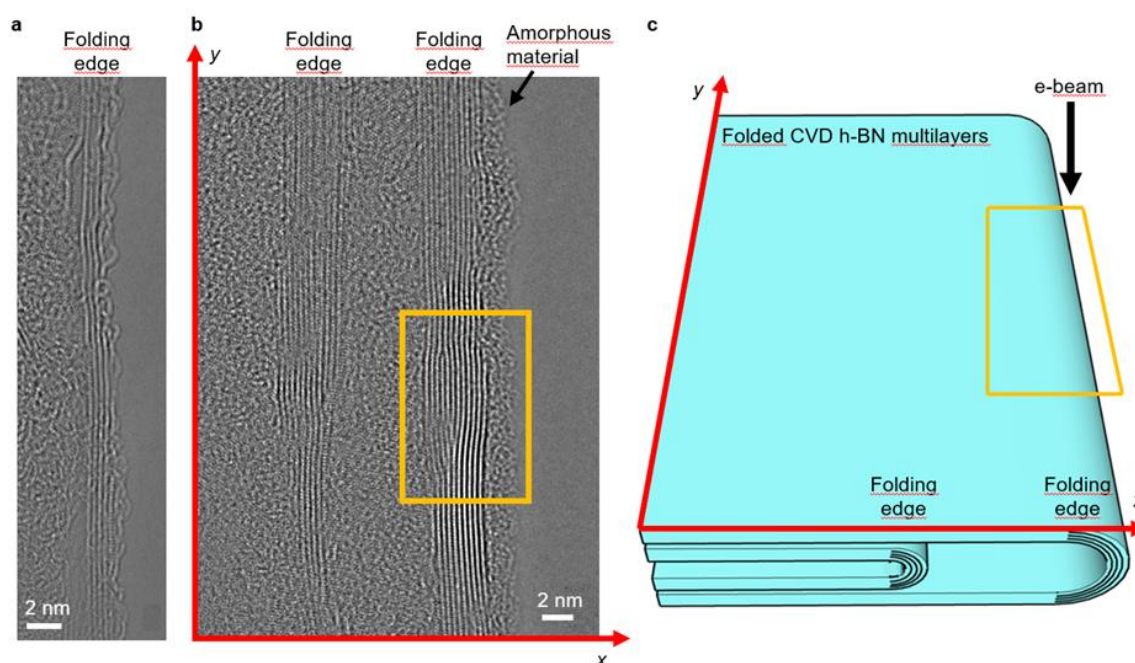

Figure S1. High-resolution TEM image of a CVD h-BN multilayer. (a) Image of two 1 nm-thick CVD-grown h-BN multilayers, which were stacked onto each other by folding. The folding edge is marked by an arrow and reveals the individual atomic h-BN layers. (b) Image several few nm-thick CVD-grown h-BN multilayers, which were stacked onto each other by folding. The folding edges are marked by arrows and reveal the individual atomic h-BN layers. (c) Illustration of the multilayer sample shown in panel (b). The yellow rectangle makes the folding edge, which corresponds to the area marked by the yellow rectangle in panel (b).

Figure S2 represents EELS spectra of B and N acquired from approximately 2x2 μm^2 area (adjusted to the diameter of the hole in the carbon film) in diffraction mode at low scattering angles around central spot in the region shown in Figure 1b of the main text. The Boron pre-edge peak at 192 eV corresponds to the transition to π^* level of hBN π-system. Its sharpness indicates (FWHM is about 0.5 eV) low degree of disturbance of π-system over the measured area.
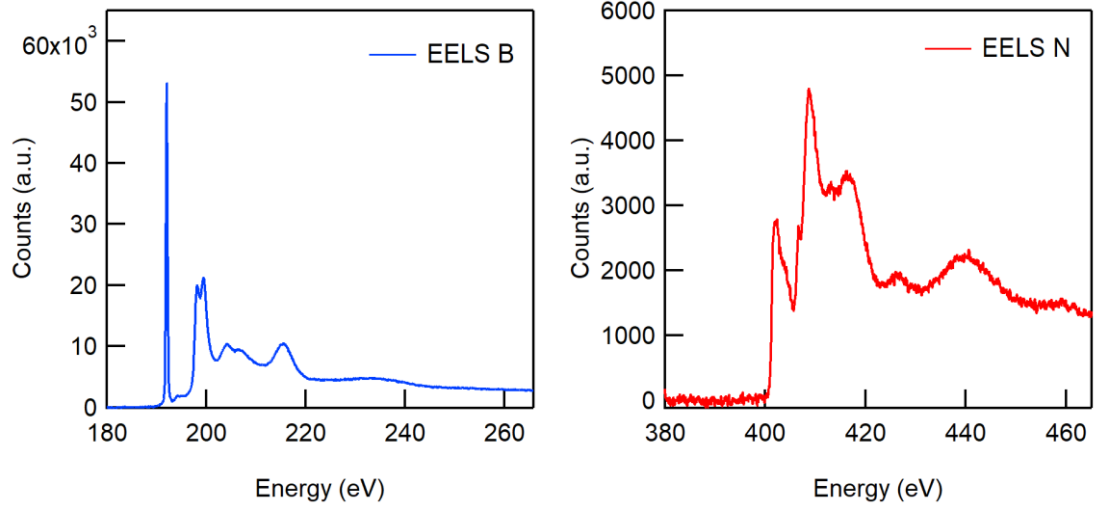
Figure S2. EELS spectra of CVD grown h-BN multilayer. (a) Spectral region of the *K* absorption edge of the Boron (B) atoms. (b) Spectral region of the *K* absorption edge of the Nitrogen (N) atoms.

Supplementary Section 2. Model for simulating the s-SNOM images of Figure 2h.

In this note we model s-SNOM images of a ML-hBN layer (i) using the conductive sheet model[1,2] to describe the polariton propagation, and (ii) including a random distribution of perfect scatterers with an anisotropic polarizability to mimic the PhP scattering at the defects. We assume that the polaritons are launched exclusively by the tip, which is treated as a vertically polarized point dipole source with a dipole moment $\mathbf{p}_0$. The polaritons propagate along the layer, scatter at the defects and eventually propagate back to the tip [located at the position $\mathbf{r} = (x, y)$], where they are scattered additionally to the incident field into the far-field radiation that is recorded by a detector. The tip-scattered field can be thus expressed as

$$E_{\text{sca}}(\mathbf{r}) \propto E_{\text{inc}} + \Delta E(\mathbf{r}), \tag{S1}$$

where E_{inc} is the incident field at the tip position and $\Delta E(\mathbf{r})$ is the total polariton field at the tip position.

Assuming that the defects are randomly distributed, monodisperse and that their size is much smaller than their mutual distance and the polariton wavelength, we model the defects (numerated *j*) as point scatterers with a polarizability tensor, $\hat{\alpha}_j$, and a dipole moment $\mathbf{p}_j$:

$$\mathbf{p}_j = \hat{\alpha}_j \mathbf{E}_{\text{p}}(\mathbf{r}_j) = \begin{pmatrix} \alpha_{j\parallel} & 0 & 0 \\ 0 & \alpha_{j\parallel} & 0 \\ 0 & 0 & \alpha_{jz} \end{pmatrix} \mathbf{E}_{\text{p}}(\mathbf{r}_j), \tag{S2}$$

where $\mathbf{r}_j$ is the position of the jth defect and $\mathbf{E}_{\text{p}}$ the field of the tip-launched polaritons at the position of the defect, which can be expressed as

$$\mathbf{E}_{\text{p}}(\mathbf{r}_j) = \hat{G}(\mathbf{r}_j, \mathbf{r}) \cdot \mathbf{p}_0 \tag{S3}$$

where $\hat{G}(\mathbf{r}, \mathbf{r}_j)$ is the Dyadic Green's function (DGF). We assume that the polarizability of the defects is in-plane isotropic, but that it can be different to the out-of-plane polarizability. Assuming that the polariton scattering between the defects is negligibly small, the total polariton field at the tip position (i.e. the tip-scattered polariton field) can be then expressed as

$$\Delta \mathbf{E}(\mathbf{r}) = \sum_j \hat{G}(\mathbf{r}, \mathbf{r}_j) \cdot \mathbf{p}_j, \tag{S4}$$

Since the polariton modes supported by the layer are transverse magnetic (TM), they comprise an out-of-plane (vertical) electric field component as well as an in-plane electric field component parallel to the wavevector, yielding an out-of-plane dipole moment, p_{jz}, and an in-plane component, $\mathbf{p}_{j||}$, parallel to the vector $\Delta \mathbf{r} = \mathbf{r}_j - \mathbf{r}$:

$$p_{jz} = \alpha_{jz} G_{zz}(|\mathbf{r}_j - \mathbf{r}|) \, p_0 \quad \text{and} \quad \mathbf{p}_{j||} = \alpha_{j||} G_{||z}(|\mathbf{r}_j - \mathbf{r}|) \frac{\mathbf{r}_j - \mathbf{r}}{|\mathbf{r}_j - \mathbf{r}|} \, p_0. \tag{S5}$$

In the following, we consider only the z-component of the polariton field at the tip position, $\Delta E_z(\mathbf{r})$, because it is the dominant field component scattered by the vertically elongated tip. Thus, by combining Equations S4 and S5 we obtain the following expression for the z-component of the total polariton field that is scattered by the tip:

$$\Delta E_z(\mathbf{r}) = p_0 \sum_j \left[\alpha_{jz} \, G_{zz}(|\mathbf{r} - \mathbf{r}_j|)^2 + \alpha_{j||} G_{||z}(|\mathbf{r} - \mathbf{r}_j|)^2 \right]. \tag{S6}$$

We can simplify Equation S6 by considering only the fundamental TM polariton mode (for hBN phonon polaritons the so-called M0 mode, which has the longest propagation length[3]) and the polariton field is recorded at fixed height. In this case, we can express the Green's function as a cylindrical wave:

$$G_{zz}(r) \sim \frac{e^{ik_{\mathrm{p}}r}}{\sqrt{r}} \quad \text{and} \quad G_{||z}(r) \sim \frac{e^{ik_{\mathrm{p}}r}}{\sqrt{r}}, \tag{S7}$$

where k_{p} is the complex-valued wavevector of the polariton mode. Thus, Equation S6 can be further simplified to the following equation:

$$\Delta E_z(\mathbf{r}) \sim \sum_j \alpha_j \frac{e^{2ik_{\mathrm{p}}|\mathbf{r} - \mathbf{r}_j|}}{|\mathbf{r} - \mathbf{r}_j|} \tag{S8}$$

where $\alpha_j = \alpha_{jz} + \alpha_{j||}$. To simulate the s-SNOM images shown in Figure 2h of the main text, we applied Equation S1 and S8 using $\Delta E(\mathbf{r}) = \Delta E_z(\mathbf{r})$, and assumed that α_j is the same for all defects.

Supplementary Section 3. Analytical expression describing the Fourier transform of s-SNOM near-field images

To use our analytical model for the analysis of the Fourier transforms (FTs) of the experimental s-SNOM images, we calculated the FT of the simulated near-field images obtained by Equation S8. We find:

$$\hat{\sigma}(\mathbf{k}) \equiv \mathcal{F}[\Delta E_z(\mathbf{r})](\mathbf{k}) \sim \sum_j \alpha_j \int d^2\mathbf{r} \, e^{i\mathbf{k}\mathbf{r}} \frac{e^{2ik_p|\mathbf{r}-\mathbf{r}_j|}}{|\mathbf{r}-\mathbf{r}_j|}. \tag{S9}$$

Shifting the coordinates in the integrand according to $\mathbf{r} \rightarrow \mathbf{r} + \mathbf{r}_j$, we obtain:

$$\hat{\sigma}(\mathbf{k}) \sim \sum_j \alpha_j e^{i\mathbf{k}\mathbf{r}_j} \int d^2\mathbf{r} \, e^{i\mathbf{k}\mathbf{r}} \frac{e^{2ik_p|\mathbf{r}|}}{|\mathbf{r}|}. \tag{S10}$$

The result of the integration reads as:

$$\hat{\sigma}(\mathbf{k}) \sim \sum_j \alpha_j e^{i\mathbf{k}\mathbf{r}_j} \frac{1}{\sqrt{k^2 - 4k_p^2}}. \tag{S11}$$

For convenience, we calculate the square of the FT absolute value, splitting k_p into real and imaginary parts:

$$|\hat{\sigma}(\mathbf{q})|^2 \sim \frac{1}{\sqrt{\left(q^2 - 4\left[(Re[q_p])^2 - (Im[q_p])^2\right]\right)^2 + 64(Im[q_p])^2(Re[q_p])^2}} \left|\sum_j \alpha_j e^{ik_0 \mathbf{q}\mathbf{r}_j}\right|^2 \tag{S12}$$

where we introduce the normalized wavevector $\mathbf{q} = \mathbf{k}/k_0$.

The first factor in Equation S12 represents a smooth envelope with a maximum at q close to twice the polariton wave vector. The square of the sum equals $S(\mathbf{k})N$, where N is the number of defects and $S(\mathbf{k}) = \frac{1}{N}\left|\sum_j \alpha_j e^{i\mathbf{q}\mathbf{k}_0 r_j}\right|^2$ is the structure factor of the disordered film. For a purely random distribution of the defects, as we assume in our modeling of the h-BN layer, it is known that $S(\mathbf{k}) \rightarrow 1$ for $N \rightarrow \infty$, which is independent of $\mathbf{k}$. In the case of a near-field image with a size much larger than the wavelength, $S(\mathbf{k})$ leads to noise on the smooth envelope, which can be seen in the FT of simulated (colored curves in Figure S3a) and experimental (black curve in Figure 3a of the main text) images. As shown in Figure S3 with simulation data, we can well fit the FT of s-SNOM images using the smooth envelope function, which is independent of the distribution and structure of the defects:

$$|\hat{\sigma}(q)|^2 \sim \frac{1}{\sqrt{\left(q^2 - 4\left[(Re[q_p])^2 - (Im[q_p])^2\right]\right)^2 + 64(Im[q_p])^2(Re[q_p])^2}}. \tag{S13}$$

Supplementary Section 4. Validation of Equation 1 of the main text via simulations

To verify that Equation 13 of the main text (Equation S13) can be applied to determine the complex-valued polariton wavevector k_p, we simulated complex-valued s-SNOM images (i.e. amplitude and phase images) of a 13 nm thick ML-hBN layer with defects of a density of 30 μm^{-2} (the same as in Figure 2h) for different illumination frequencies ν. For the dielectric function of the layer we used that of ML-hBN. FT of the images was performed and radial line profiles, $|\hat{\sigma}(k_x, k_y)|^2$, were extracted (colored curves in Figure S1a). They can be perfectly fitted by applying Equation 1 of the main text (Equation S13), yielding the complex-valued polariton wavevector $k_p = k_p' + ik_p''$ and subsequently the

polariton dispersion $v\left(k_{\mathrm{p}}^{'}/k_0\right)$ and polariton lengths $L_{\mathrm{p}}(v) = 1/k_{\mathrm{p}}^{''}$ (colored symbols in Figure S3b and c, respectively). The fitting results excellently match the analytically calculated (see Methods) phonon polariton dispersion and propagation lengths (black solid lines in Figure S3b and c) of a 12 nm thick hBN layer with the same dielectric function as the one used for simulating the s-SNOM image. Figure S3 thus clearly demonstrates the validity of Equation 1 of the main text (Equation S13) to determine the complex-valued polariton momentum from FTs of complex-valued simulated s-SNOM images.
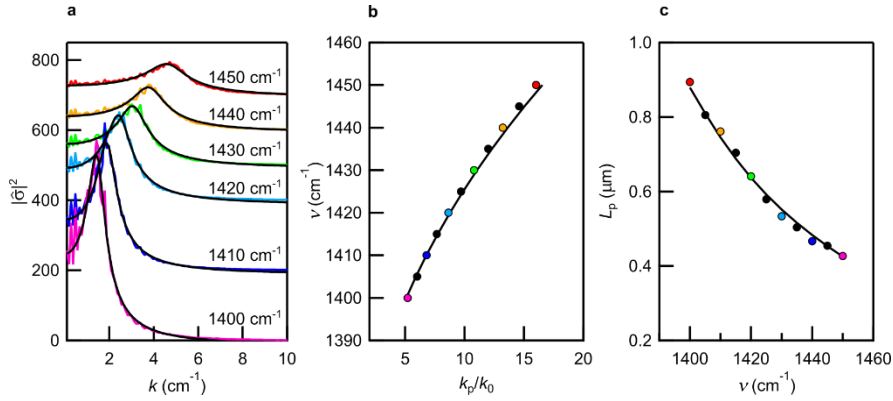

Figure S3. Extraction of phonon polariton dispersion and propagation lengths from Fourier transform of simulated s-SNOM images. (a) Colored curves: Radial profiles of the Fourier transform of simulated complex-valued s-SNOM images at different illumination frequencies, $|\hat{\sigma}(k_x, k_y)|^2$, assuming a 13 nm thick h-BN layer with defects of a density of $30/\mu m^2$. Black curves: Fitting based on Equation 1 of the main text (Equation S13). (b,c) Symbols show the phonon polariton dispersion and propagation lengths $L_{\mathrm{p}}(v)$ obtained from panel (a). Solid line shows the analytical phonon polariton dispersion $v\left(k_{\mathrm{p}}^{'}/k_0\right)$ and propagation lengths of a 12 nm thick h-BN slab without defects.

Supplementary Section 5. Comparison of FTs of real and complex-valued s-SNOM images

Figure S4 shows s-SNOM images of a 13 nm thick ML-hBN at 1430 cm^{-1}, similar to those presented in Figure 2f of the main text. The interferometric detection of the s-SNOM allows us to record the phase φ_3 and amplitude s_3 images (Figure S4a and b top), from which we can calculate the complex-valued s-SNOM signal $\sigma_3 = s_3 e^{i\varphi_3}$ and images showing the real and imaginary parts, $\mathrm{Re}(\sigma_3)$ and $\mathrm{Im}(\sigma_3)$, respectively (Figure S4c and d top). All the images show random interference fringes. However, the periodicity of the fringes is partially different, which can be verified with the FT of the images (Figure S4a-d bottom). We observe that the FT maps of the s_3 and $\mathrm{Re}(\sigma_3)$ images show rings with larger diameters than the FT maps of the φ_3 and $\mathrm{Im}(\sigma_3)$ images. Further, the s_3 and $\mathrm{Re}(\sigma_3)$ images show a bright disk-like feature in the center, which is absent in the the φ_3 and $\mathrm{Im}(\sigma_3)$ images. Typically, the polariton momentum is determined as the radius of the ring observed in the FT of polariton images.[4] Since the ring diameter is different in the various FTs, measuring the ring radius thus eventually does not provide the correct result. For that reason, we performed FT of complex-valued s-SNOM images and fitted the radial line profiles with Equation 1 of the main text. The validity of the procedure is demonstrated in Supplementary Section 4.
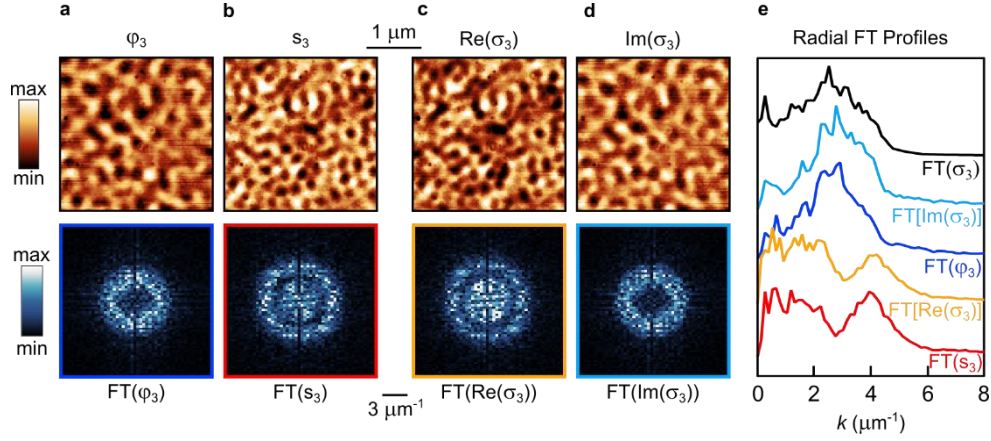
Figure S4. Fourier transforms of real valued signals. (a-d) Top: s-SNOM images showing phase φ_3, amplitude s_3, real part $\mathrm{Re}(\sigma_3)$ and imaginary part $\mathrm{Im}(\sigma_3)$ of the near-field signal. Bottom: Fourier transforms of the s-SNOM images. (e) Radial profiles extracted from the FT maps shown in panels a to d. Black curves shows the square of the Fourier transform of the complex-valued s-SNOM image, $|\mathrm{FT}(\sigma_3)|^2$.

Supplementary Section 6. Calculation of the reflection phase of propagating PhPs at hBN edges

To calculate the PhP reflection phase θ at hBN edges (used to obtain the Fabry-Perot model results shown in Figure 5 of the main text), we performed full-wave numerical simulations using the COMSOL Multiphysics software package. We assumed a 13 nm thick ML-hBN and excited via a so-called numerical port a plane PhP wave propagating along the layer. The PhP is back-reflected at an edge at a distance L from the port, yielding interference between forward and backward propagating PhPs, as can be seen in the resulting field distribution shown in Figure S5a. The back-reflected field is measured at the position of the port and normalized to the excitation field, yielding the complex-valued reflection coefficient S_{11} (S-matrix formalism), which is given by

$$S_{11} = \frac{\int_{\mathrm{port}}\big((\mathbf{E}-\mathbf{E_i^*})\cdot\mathbf{E_i^*}\big)dA}{\int_{\mathrm{port}}(\mathbf{E_i}\cdot\mathbf{E_i^*})dA}, \tag{S14}$$

where $\mathbf{E_i}$ is the initial polariton field launched by the port, $\mathbf{E}$ is the total field (including the initial and back-reflected polariton field), and dA is an element of the port surface. Assuming that only the initial and the back-reflected polaritons contribute to the total field $\mathbf{E}$ at the port, we can write $S_{11} = e^{i2k_p L}e^{i\theta}$, where k_p is the PhP wavevector. The PhP refection phase is subsequently obtained as

$$\theta = \mathrm{Arg}[S_{11}/e^{i2k_p L}]. \tag{S15}$$

Figure S5b and c show that θ is about 0.32π, nearly independent of L and wavenumber v. The weak oscillations of the phase observed in Figure S5b (corresponding to an uncertainty of less than $\pm0.02\pi$) can be attributed to numerical errors, as well as to

polariton scattering at the sample edge into free-space waves and higher-order polariton modes that are not considered in Equation S15.
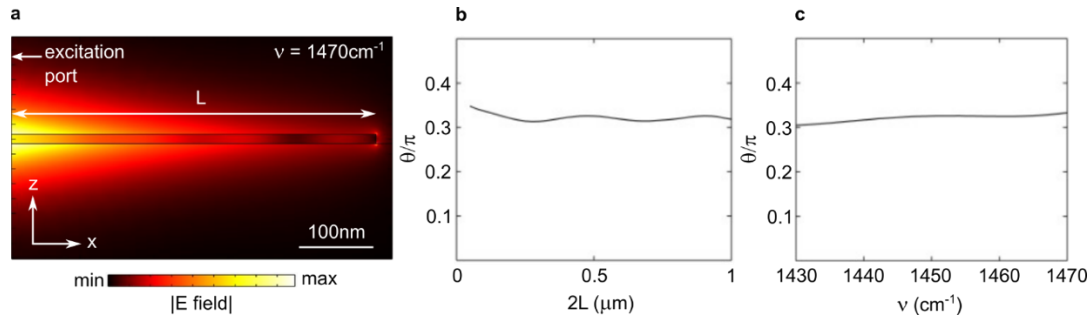

Figure S5. PhP reflection Phase. (a) Simulated near-field amplitude distribution of a PhP wave in a 13 nm thick CVD-grown h-BN layer, excited on the left side (via a so-called port in COMSOL) and reflected by the h-BN edge on the right side. (b) PhP refection phase as a function of distance L between port and h-BN edge for $\nu = 1470$ cm^{-1}. (c) PhP refection phase as a function of wavenumber for $L = 500$ nm.

Supplementary section 7. Reproducibility of PhP observation on different CVD-grown hBN layers

To demonstrate the reproducibility of PhPs on CVD-grown hBN layers, we show in Figure S6 our results obtained with samples named hBN6 and S1. The main text shows results obtained with the sample named S3. Each of the samples was grown in a separate process, but with similar process parameters.

In Figure S6a and b we present topography z, near-field amplitude s_3, near-field phase φ_3, and the square modulus of FT of the complex-valued near-field image, $|FT(\sigma_3)|^2$, of sample hBN6, which is a 6 nm-thick hBN layer (one ML-hBN layers) on a CaF$_2$ substrate. In Figure S6b we show the results obtained with sample S1, which is a 11 nm-thick hBN layer (two stacked ML-hBN layers) on a SiO$_2$/Si substrate (sample S1). Similar to the s-SNOM images shown in Figure 2 of the main text, we observe random PhP interference fringe patterns in the near-field amplitude and phase images. Accordingly, the FTs of the complex-valued near-field images reveal a bright ring. The fits (red curves in Figure S6c and d) of the radial profiles of the FTs (black curves in Figure S6c and d) yield – analogously to the main text – the complex-valued PhP wavevectors k_p^{exp}, which are shown in Figure S6e and f (red text). They agree well with calculations of the PhP wavevectors k_p^{calc} (blue text in Figure S6e and f), which consider the specific layer thickness and substrate. For all calculations we used the dielectric function reported in Figure 1e of the main text (obtained from sample S3). The good agreement between the measured and calculated wavevectors for all samples (S1, S3, and hBN6) using the same dielectric function (obtained from S3) demonstrates the good reproducibility of the hBN layer growth and the PhP properties.
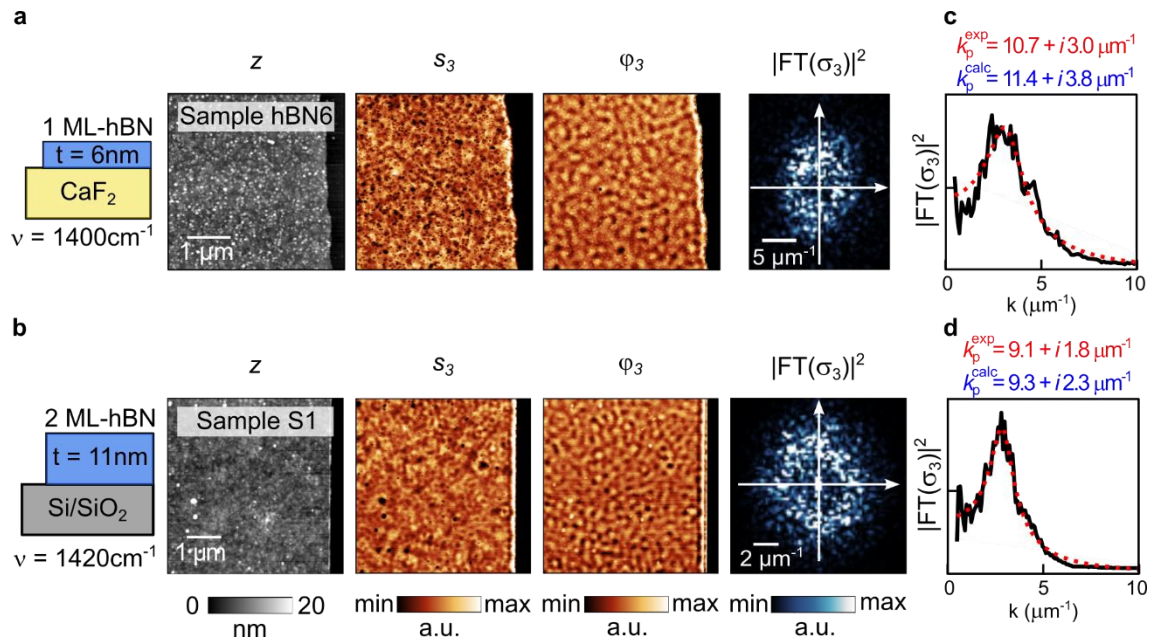
Figure S6. s-SNOM study of different hBN samples. (a,b) From left to right: Topography z, near-field amplitude s_3 and phase φ_3 images, and square modulus of the FT of the complex-valued near-field images. (a) Sample S1: 6 nm thick hBN layer (one ML-hBN layer) on a CaF_2 substrate, recorded at 1400 cm^{-1}. (b) Sample hBN6: 11 nm thick hBN layer (two stacked ML-hBN layers) on a SiO_2/Si substrate, recorded at 1420 cm^{-1}. (c,d) Radial profiles (black curves) extracted from the FT maps shown in panels a and b. Red curves show fits.

References

[1] J. S. Gomez-Diaz, M. Tymchenko, A. Alù, *Phys. Rev. Lett.* **2015**, *114*, 233901.

[2] A. Y. Nikitin, in *World Scientific Handbook of Metamaterials and Plasmonics: Volume 4: Recent Progress in the Field of Nanoplasmonics*, World Scientific, **2018**, pp. 307–338.

[3] S. Dai, Z. Fei, Q. Ma, A. S. Rodin, M. Wagner, A. S. McLeod, M. K. Liu, W. Gannett, W. Regan, K. Watanabe, T. Taniguchi, M. Thiemens, G. Dominguez, A. H. C. Neto, A. Zettl, F. Keilmann, P. Jarillo-Herrero, M. M. Fogler, D. N. Basov, *Science* **2014**, *343*, 1125.

[4] N. Zhang, W. Luo, L. Wang, J. Fan, W. Wu, M. Ren, X. Zhang, W. Cai, J. Xu, *Nat Commun* **2022**, *13*, 983.